*applied sciences*

MDPI

*Article*

# A New Neutron Gamma Density Algorithm Based on Drill-Collar Inelastic Gamma Information

**Tian Xie [1,2], Quanying Zhang [1,2,*], Chao Yuan [3], Guobin Liu [1,2], Huichuan Li [1,2] and Yin Huang [1,2]**

[1] Key Laboratory of Exploration Technologies for Oil and Gas Resources (Yangtze University), Ministry of Education, Wuhan 430100, China
[2] College of Geophysics and Petroleum Resources, Yangtze University, Wuhan 430100, China
[3] PetroChina Oil, Gas & New Energies Company, Beijing 100007, China
* Correspondence: zhangqy@yangtzeu.edu.cn

### Featured Application

This work can provide guidance for the application of neutron gamma density technology in gas-bearing formations and high-salinity formations.

### Abstract

Neutron gamma density (NGD) logging, as a safer and more environmentally friendly density logging method, has been applied in logging while drilling (LWD) for many years. However, most NGD algorithms have low density sensitivity and exhibit significant errors in the presence of gas and high-salinity water. To address the above issues, the inelastic gamma information of the drill collar is simulated by the Monte Carlo method, and its impact on NGD sensitivity and the results are studied. Using the drill-collar inelastic gamma information, a new neutron gamma density algorithm is proposed. The study shows that the drill-collar inelastic gamma information occupies a large proportion of the total inelastic gamma count recorded by the detector, which reduces the sensitivity of the NGD algorithms using the total inelastic gamma information. By eliminating the contribution of the drill collar from the total inelastic gamma count, the density sensitivity of the NGD algorithms can be significantly improved. In addition, the drill-collar inelastic gamma information is closely related to high-energy fast neutrons and can be used to correct the fast neutron distribution in NGD logging. The new NGD algorithm, utilizing the drill-collar inelastic gamma information, has excellent performance in the presence of gas and high-salinity water. However, similar to the other algorithms, the new algorithm is still affected by other environmental factors such as borehole, lithology, and shale. Furthermore, this new algorithm does not require any additional modifications to existing NGD tools and can work with other NGD algorithms.

**Keywords:** neutron gamma density; drill collar; inelastic gamma; density sensitivity; gas-bearing formation; high-salinity water

Check for updates

Academic Editor: Nikolaos Koukouzas

Received: 24 June 2026
Revised: 9 July 2026
Accepted: 9 July 2026
Published: 13 July 2026

**Copyright:** © 2026 by the authors. Licensee MDPI, Basel, Switzerland. This article is an open access article distributed under the terms and conditions of the Creative Commons Attribution (CC BY) license.

## 1. Introduction

Traditional density logging employs Cs-137 chemical sources to measure formation density. This method can not only harm the health of field personnel but may also cause environmental pollution. Especially during LWD operations, the accidental downhole loss of chemical sources may lead to severe ecological safety issues. In contrast, NGD logging utilizes a D–T source,

significantly enhancing operational safety and environmental friendliness while ensuring measurement accuracy [1–4]. With stringent safety requirements for radioactive logging, replacing chemical sources with controllable sources has become an inevitable trend [5–8].

In the late 20th century, Odom and Wilson proposed the concept of NGD logging, which used inelastic gamma information to calculate formation density [9–11]. However, studies have shown that the generation and distribution of inelastic gamma rays are closely related to neutron transport effects. Therefore, while using inelastic gamma information as the main parameter for density calculation, it is also necessary to correct for the fast neutron distribution [12–16]. According to different correction parameters, existing NGD algorithms are divided into the NGD algorithm based on fast neutrons (FNGD), the NGD algorithm based on captured gamma (CNGD), and the NGD algorithm based on thermal neutrons/epithermal neutrons (TNGD).

The FNGD directly utilizes fast neutrons to correct the fast neutron distribution. The measurement results of this algorithm are less affected by environmental factors [17–19]. However, existing detectors cannot effectively obtain information about high-energy fast neutrons. This makes the FNGD difficult to apply in practical production. To address this problem, existing NGD algorithms can only indirectly characterize fast neutrons using capture gamma, epithermal neutrons, or thermal neutrons. The CNGD uses capture gamma information to correct the fast neutron distribution [20]. The advantage of this algorithm is the stability of the capture gamma count and the maturity of detection technology. Quirein used capture gamma information recorded by the PNC tool to correct the fast neutron distribution of inelastic gamma, achieving more accurate density measurements [21–23]. The TNGD utilizes epithermal or thermal neutrons to characterize fast neutrons. This is because both epithermal and thermal neutrons are formed after fast neutrons are slowed down, and both types of particles can reflect the distribution characteristics of fast neutrons in the formation. Schlumberger's NeoScope instrument corrects the fast neutron distribution by using a combination of thermal and epithermal neutron information [24–28]. Both CNGD and TNGD can achieve density measurement. However, information such as capture gamma and thermal neutrons only indirectly characterizes fast neutrons, and this process will introduce the different environmental influences in the NGD results. As a result, all the NGD algorithms except the FNGD exhibit obvious density measurement errors in gas-bearing formations and high-salinity formations, failing to meet the requirements of practical production applications. In addition, current NGD algorithms directly use total inelastic gamma information for density calculation. However, the drill collar also generates numerous inelastic gamma rays in LWD [29]. The detector records a large amount of drill-collar inelastic gamma, reducing the proportion of formation information and leading to a decrease in density sensitivity.

To address the above issues, this paper proposes a new neutron gamma density algorithm based on drill-collar inelastic gamma information. Utilizing the numerical simulation method, the characteristics of drill-collar inelastic gamma are studied. The NGD sensitivity is improved by subtracting the drill-collar gamma information from the total inelastic gamma count. Furthermore, by using drill-collar inelastic gamma to correct fast neutron distribution, the poor performance in gas-bearing and high-salinity formations is well resolved. In addition, other borehole and formation factors are also studied.

## 2. Method and Theory

### 2.1. Data Processing for the NGD Algorithms

The distribution of high-energy (1–14 MeV) fast neutrons in formation can be given as follows [30]:

$$\phi_{hn} = \frac{S_0}{4\pi r^2} e^{-\Sigma_s r} \quad (1)$$

where $\Sigma_s$ is the high-energy fast-neutron-scattering cross-section, $S_0$ is the neutron source strength, and $r$ is the distance from the source.

The distribution of gamma rays in the formation is described by the approximation in Equation (2), which reduces the integral following ref. [31]:

$$\phi_{ir}(R) = \frac{\int_0^\infty k\Sigma_{ir}\phi_{hn}e^{-\mu|r-R|}dr}{4\pi R^2} \approx \frac{k\Sigma_{ir}S_0}{4\pi R^2}e^{-R(1-\alpha)\Sigma_s}e^{-R\rho\alpha\mu_m} \quad (2)$$

where $\Sigma_{ir}$ is the inelastic scattering cross-section, $R$ is the distance from the detector to the neutron source, $\rho$ is the formation density, $k$ is the gamma photon count for each inelastic collision, $\alpha$ is a constant which is related to $R$, and $\mu_m$ is the mass attenuation coefficient.

Assuming the source distances of the NGD instrument are $d_1$ and $d_2$, Equation (3) gives the mathematical relationship of inelastic gamma count ratio, formation density, and high-energy fast-neutron-scattering cross-section:

$$\ln\frac{N_{ir1}}{N_{ir2}} = \ln\frac{d_2}{d_1} - [d_1(1-\alpha_1) - d_2(1-\alpha_2)]\Sigma_s - [d_1\alpha_1 - d_2\alpha_2]\rho\mu_m \quad (3)$$

where $N_{ir1}$ is the near detector count and $N_{ir2}$ is the far detector count.

Since $d_1$, $d_2$ and $\alpha_1$, $\alpha_2$ are constants, $\rho$ can be expressed as

$$\rho = A \times \ln\frac{N_{ir1}}{N_{ir2}} + B \times \Sigma_s + C \quad (4)$$

where $A$, $B$, and $C$ are calibration coefficients.

Based on the particle type used to characterize $\Sigma_s$, current NGD algorithms can be divided into four categories: the FNGD, TNGD, ENGD, and CNGD algorithms. Table 1 shows several typical density algorithms and disadvantages for different NGD algorithms [32].

**Table 1.** Different NGD algorithms.

| Algorithm | Particle Type | Density Algorithm | Disadvantage |
|---|---|---|---|
| FNGD | fast neutrons | $\rho = A \times \ln\frac{N_{ir1}}{N_{ir2}} + B \times \ln N_f + C$ | Difficult to detect high-energy fast neutrons |
| TNGD | thermal neutrons | $\rho = A \times \ln\frac{N_{ir1}}{N_{ir2}} + B \times \ln\frac{N_{t1}}{N_{t2}} + C$ | Thermal neutrons primarily reflect the hydrogen index; strongly distorted by the excavation effect in gas; also sensitive to salinity |
| ENGD | epithermal neutrons | $\rho = A \times \ln\frac{N_{ir1}}{N_{ir2}} + B \times \ln N_{epi} + C$ | Susceptible to gas influence |
| CNGD | capture gamma | $\rho = A \times \ln(\frac{N_{ir1}}{N_{ir2}} + B \times \ln\frac{N_{c1}}{N_{c2}}) + C$ | Sensitive mainly to salinity (Cl has a large capture cross-section that dominates the capture gamma); also affected in gas via thermal-neutron dependence |

Here, $N_f$ is the fast neutron count; $N_{t1}$ and $N_{t2}$ are the thermal neutron count of near and far detectors; $N_{epi}$ is the epithermal neutron count; and $N_{c1}$ and $N_{c2}$ are the capture gamma count of near and far detectors.

Among these algorithms, although the FNGD has good performance in gas-bearing formations and high-salinity formations, the high-energy fast neutron is difficult to detect. That is why the NGD tool with the FNGD is rare. As a result, common NGD tools must adopt the TNGD, ENGD, and CNGD, which leads to significant density errors in the presence of gas and high-salinity water.

Density sensitivity is a very important index for density logging. High sensitivity means that the NGD tool is more sensitive to changes in formation density and can provide

more accurate density results. According to the density algorithms in Table 1, the specific expression of the NGD sensitivity is shown in Equation (5):

$$S = \frac{dy}{d\rho_a} \cdot \frac{\rho_a}{y} \tag{5}$$

where $S$ is the normalized relative sensitivity, y is the inelastic gamma count ratio of each algorithm, and $\rho_a$ is the calculated density. The absolute error is used to evaluate the application effect of the NGD algorithms. The formula for calculating absolute error is shown in Equation (6):

$$\Delta\rho = |\rho_a - \rho_b| \tag{6}$$

where $\Delta\rho$ is the absolute error of density results, $\rho_b$ is the actual density, and $\rho_a$ is the calculated density.

### 2.2. NGD Algorithm Using Drill-Collar Information

The drill collar occupies 90% of the borehole space, and its material has a high inelastic scattering cross-section, which leads to the generation of numerous inelastic gamma rays by the drill collar. The presence of drill-collar inelastic gamma rays reduces the proportion of formation density information in the detector, thus decreasing the sensitivity to formation density. Meanwhile, the production of drill-collar inelastic gamma rays is closely related to fast neutrons and can be used for fast neutron distribution correction. Therefore, studying the characteristics of drill-collar inelastic gamma information is of great significance for improving the NGD algorithm.

#### 2.2.1. Feasibility of Acquiring the Drill-Collar Inelastic Gamma Information

As we know, obtaining inelastic gamma information from the drill collar is a challenging task, and it demands energy-spectrum analysis techniques for elemental logging.

Fortunately, the newest NGD tool of Schlumberger makes this possible. The NGD tool adopted a new design of a $LaBr_3$ short-spacing detector, which can provide high-resolution energy-spectrum measurements, and it can obtain accurate formation element information for correcting sourceless density. In the above study, the researchers clearly stated that the new $LaBr_3$-based spectroscopy measurement obviously reduces the uncertainty of the iron dry weight (for the shale correction) by lowering the tool background and its variability as a function of the environment. It was noted that the drill-collar gamma information is nearly equivalent to the tool background in LWD. This means that obtaining the drill-collar inelastic gamma information in the total gamma spectrum is achievable by using current NGD technology.

#### 2.2.2. Acquisition of the Drill-Collar Inelastic Gamma Information

To investigate the impact of the drill-collar inelastic gamma information on the NGD algorithms, this study employs spectral analysis techniques to obtain this information [33–35]:

$$\begin{cases} y_{11}x_1 + y_{12}x_2 \cdots + y_{1m}x_m + y_{1m+1}x_{m+1} = z_1 \\ y_{21}x_1 + y_{22}x_2 \cdots + y_{2m}x_m + y_{2m+1}x_{m+1} = z_2 \\ \cdots \\ y_{n1}x_1 + y_{n2}x_2 \cdots + y_{nm}x_m + y_{nm+1}x_{m+1} = z_n \end{cases} \tag{7}$$

where $n$ is the number of channels of the inelastic gamma spectrum recorded by the tool; $m$ is the number of element types; $y_{nm}$ represents the probability distribution of the count in the $n$th energy channel for the inelastic standard spectrum of the $m$th element; $x_m$ represents

the yield of the $m$th element; and $z_n$ represents the count in the $n$th energy channel for the total inelastic gamma spectrum.

#### 2.2.3. New NGD Algorithm Based on Drill-Collar Information

The proportion of formation density information is increased by subtracting the effect of the drill collar from the total inelastic count:

$$N_{irf} = N_{ir} - N_{ird} \tag{8}$$

where $N_{irf}$ is the formation inelastic gamma count; $N_{ir}$ is the total inelastic gamma count; and $N_{ird}$ is the drill-collar inelastic gamma count.

The generation of the drill-collar inelastic gamma is closely related to high-energy fast neutrons. The drill-collar inelastic gamma inherits the characteristics of fast neutrons, and it can be used to correct the fast neutron distribution while being largely insensitive to gas-bearing and high-salinity formations, in contrast to capture gamma or thermal neutrons, which are strongly affected by the excavation effect and the high capture cross-section of chlorine. The relationship between Σs and drill-collar inelastic gamma can be given by Equation (9):

$$\Sigma_s = f(N_{ird}) \tag{9}$$

A new NGD algorithm is proposed by utilizing formation inelastic gamma, which eliminates the influence of the drill collar to calculate density, and by introducing drill-collar inelastic gamma for the fast neutron distribution correction. This new NGD algorithm is called a new neutron gamma density algorithm based on drill-collar inelastic gamma information (abbreviated as DNGD). Equation (10) demonstrates the specific form of the new NGD algorithm.

$$\rho = A \times \ln\left(\frac{N_{ir1} - N_{ird1}}{N_{ir2} - N_{ird2}}\right) + B \times f(N_{ird}) + C \tag{10}$$

Here, $N_{ir1}$ is the total inelastic gamma count of the near detector, $N_{ir2}$ is the total inelastic gamma count of the far detector, $N_{ird1}$ is the drill-collar inelastic gamma count of the near detector, and $N_{ird2}$ is the drill-collar inelastic gamma count of the far detector.

## 3. Simulation and Data Processing

### *3.1. Monte Carlo Method*

A numerical simulation model of the NGD logging tool was developed using the Monte Carlo method. As shown in Figure 1, the model consists of a D-T neutron source, two $LaBr_3$ gamma detectors, a drill collar, and the formation.

Both gamma detectors use $LaBr_3$ crystals, each 5.7 cm in diameter and 10 cm in length. The gamma detectors are located at distances of 25 cm and 70 cm from the neutron source. The reason for using the $LaBr_3$ detector is that it has a higher resolution than the NaI detector. This allows the detector to more clearly identify the characteristic energy peaks of the elements, which is very beneficial for obtaining drill-collar inelastic gamma information. The drill collar is made of a non-magnetic steel, 19 cm in diameter, with a density of 7.76 g/cm$^3$; the tool housing is made of 17–4PH stainless steel, 0.5 cm thick, with a density of 7.78 g/cm$^3$. The borehole size is 20 cm, and the borehole is filled with freshwater; the formation is modeled as a water-saturated limestone with porosity ranging from 1% to 40%.

Fast neutron information can be effectively recorded in numerical simulations. To study the relationship between the drill-collar inelastic gamma and the fast neu-

trons, the gamma detector can be replaced with a fast neutron detector to record fast neutron information.

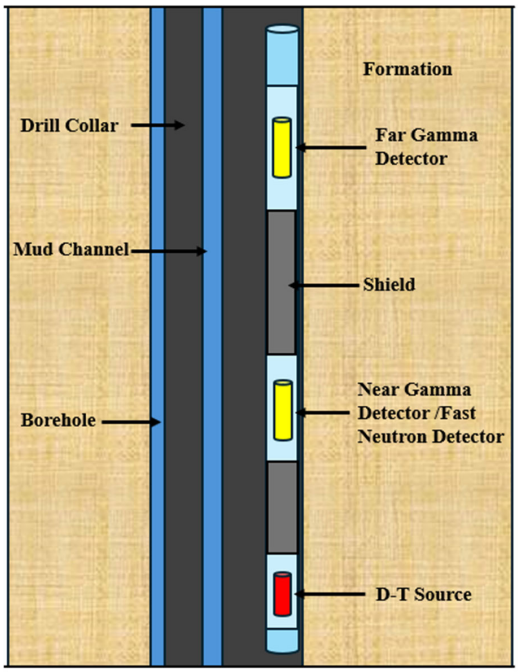



**Figure 1.** Simulation model example.

The simulation uses $6 \times 10^8$ source neutrons. The D-T neutron tube emits 14.1 MeV neutrons with a pulse width of 20 μs and a period of 400 μs. The recording time windows are 0–20 μs for the fast neutrons and inelastic gamma and 30–400 μs for the capture gamma. The energy ranges are 1–14.1 MeV for the fast neutrons and 0.01–8.5 MeV for the gamma detectors, with 256 energy channels.

### *3.2. Characteristics of the Drill-Collar Inelastic Gamma*

#### 3.2.1. Drill-Collar Inelastic Gamma Spectrum

Figure 2 shows two different inelastic gamma spectrums. Compared to the total inelastic gamma spectrum, the drill-collar inelastic gamma spectrum has the following characteristics: the absence of characteristic peaks of formation elements such as carbon, oxygen, and calcium. It also exhibits inelastic characteristic peaks of metallic elements in the energy range of 0.8 to 1.5 MeV.

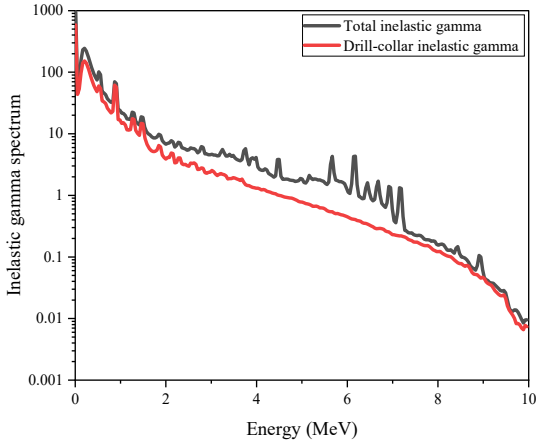



**Figure 2.** Comparison of different inelastic gamma spectra.

3.2.2. The Effect of Drill-Collar Inelastic Gamma on NGD Algorithm

The drill-collar inelastic gamma count accounts for 48% to 72% of the total inelastic gamma count. As shown in Figure 3, due to sufficient fast neutrons, the proportion of drill-collar inelastic gamma by the near detector is high and stable. However, the number of fast neutrons reaching the far detector is affected by formation porosity. Higher formation porosity increases the ability of the formation to decelerate neutrons, resulting in fewer fast neutrons reaching the far detector. Therefore, the proportion of drill-collar inelastic gamma at the far detector decreases with increasing porosity.

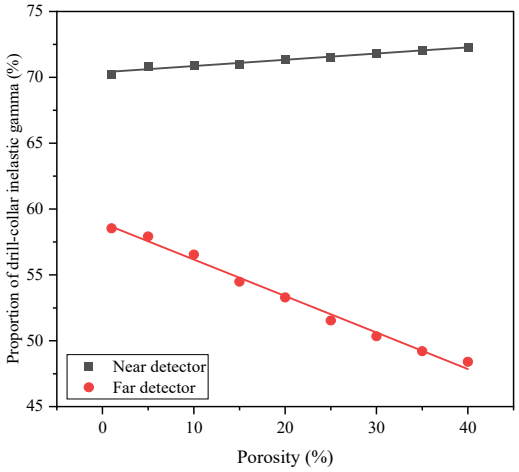



**Figure 3.** Proportion of drill-collar inelastic gamma.

The presence of drill-collar inelastic gamma reduces the proportion of formation information and is a significant factor in the decrease in density sensitivity. To increase the proportion of formation information, the formation inelastic gamma count can be obtained by subtracting the influence of drill collar from the total inelastic gamma count. The response laws of the formation inelastic gamma are shown in Figure 4a. The relative sensitivity of the two inelastic gamma count ratios is calculated using Equation (5). The calculation results are shown in Figure 4b. Traditional count ratios are almost insensitive to density at the high-density end, while formation inelastic gamma count ratios remain highly sensitive throughout the range.

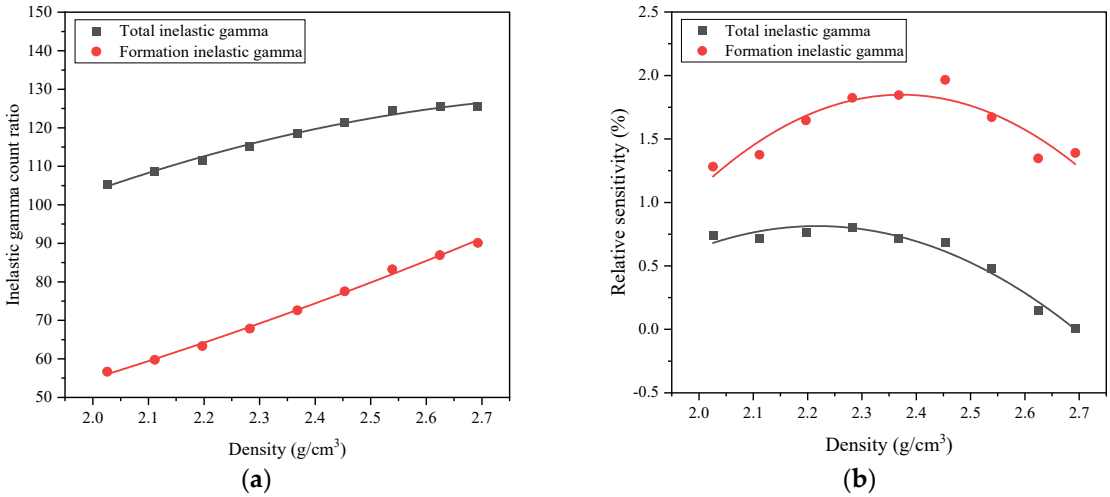



**Figure 4.** Comparison between the total inelastic gamma and the formation inelastic gamma. (**a**) Variation in the inelastic gamma count ratio with density. (**b**) Comparison of the relative sensitivity of the formation inelastic gamma and drill-collar inelastic gamma.

The high-energy fast neutron count is recorded by replacing the gamma detector with a fast neutron detector. As shown in Figure 5, the recorded fast neutron count shows a clear linear relationship with the drill-collar inelastic gamma count. Whether in gas-bearing formations or high-salinity formations, the drill-collar inelastic gamma count can also characterize fast neutron count.

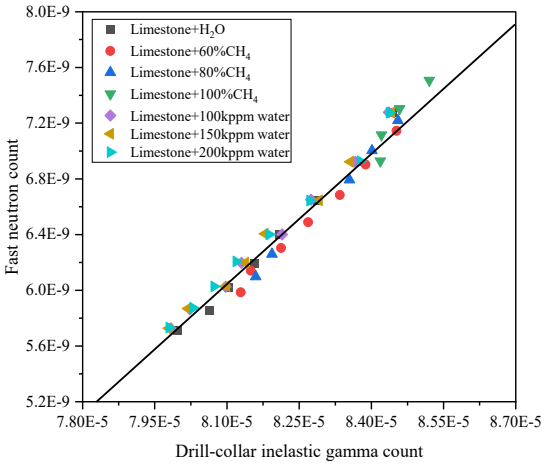



**Figure 5.** Relationship between drill-collar inelastic gamma count and fast neutron count.

Linear fitting was performed on the drill-collar inelastic gamma count and fast neutron count, and the results are as follows:

$$N_f = 3.256 \times 10^{-4} N_{ird1} - 2.03 \times 10^{-8} \quad (11)$$

The linear fitting result, $R^2$ = 0.9773, confirms a very strong linear correlation between the two physical parameters. This demonstrates that the drill-collar inelastic gamma count can characterize the fast neutron count.

### *3.3. Density Algorithm and Sensitivity Analysis*

By the numerical simulation method, the simulation model can record inelastic gamma information, captured gamma information, and fast neutron information. This study presents a comparative study of the DNGD with the CNGD and FNGD. These NGD algorithms are calibrated in freshwater-saturated limestone with different densities and HI (hydrogen index). The formation is a water-saturated limestone. The formation HI is set to 0.01, 0.05, 0.10, 0.15, 0.20, 0.25, 0.30, 0.35 and 0.40. For a constant formation HI, the formation density is additionally varied in a small range (±0.20 g/cm$^3$). The formation conditions are listed in Table 2.

**Table 2.** Parameters of limestone with different densities and HI.

| Limestone with Different Densities and HI | | | |
|---|---|---|---|
| **HI** | **ρ (g/cm$^3$)** | **ρ − 0.02 g/cm$^3$** | **ρ + 0.02 g/cm$^3$** |
| 0.01 | 2.6929 | 2.4929 | 2.8929 |
| 0.05 | 2.6245 | 2.4245 | 2.8245 |
| 0.10 | 2.5390 | 2.3390 | 2.7390 |
| 0.15 | 2.4535 | 2.2535 | 2.6535 |
| 0.20 | 2.3680 | 2.1680 | 2.5680 |
| 0.25 | 2.2825 | 2.0825 | 2.4825 |
| 0.30 | 2.1970 | 1.9970 | 2.3970 |
| 0.35 | 2.1115 | 1.9115 | 2.3115 |
| 0.40 | 2.0260 | 1.8260 | 2.2260 |

The results of the three NGD algorithms are shown in Figure 6. All algorithms show good results in freshwater-saturated limestone.

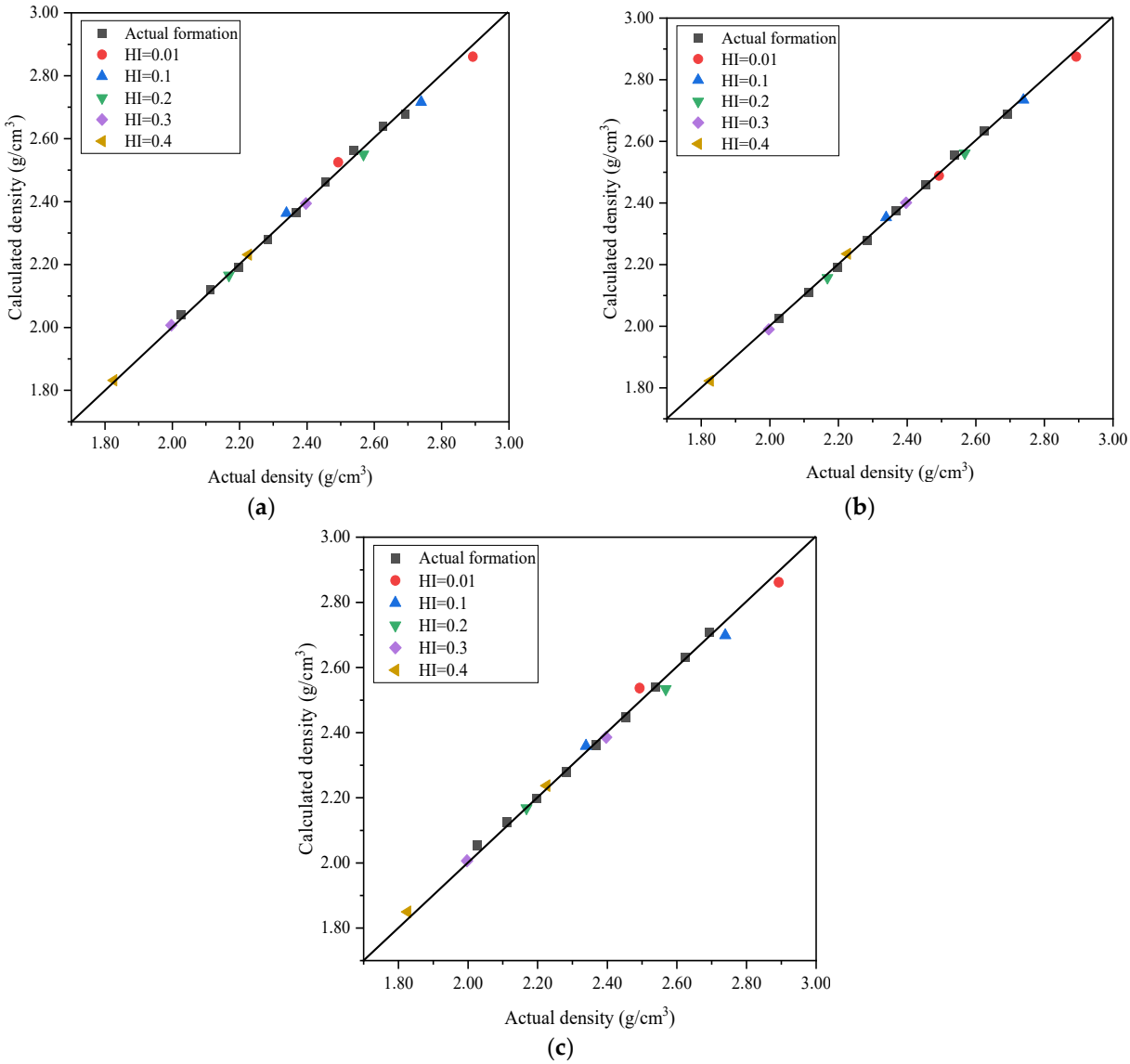



**Figure 6.** Calculated density results for limestone with different densities and HI. (**a**) Results of DNGD application in freshwater-saturated limestone. (**b**) Results of CNGD application in freshwater-saturated limestone. (**c**) Results of FNGD application in freshwater-saturated limestone.

The density algorithm for the DNGD is as follows:

$$\rho = 0.86 \times \ln\left(\frac{N_{ir1} - N_{ird1}}{N_{ir2} - N_{ird2}}\right) + 4.23 \times \ln N_{ird1} + 38.50 \tag{12}$$

The density algorithm for the CNGD is as follows:

$$\rho = 1.17 \times \ln\left(\frac{N_{ir1}}{N_{ir2}} - 0.56 \times \ln\frac{N_{c1}}{N_{c2}}\right) - 2.88 \tag{13}$$

The density algorithm for the FNGD is as follows:

$$\rho = 1.02 \times \ln\frac{N_{ir1}}{N_{ir2}} + 1.65 \times \ln N_f + 28.73 \tag{14}$$

Table 3 shows three NGD algorithms used for calculations on water-saturated limestone with porosities of 1–40%. The DNGD exhibits the highest sensitivity throughout, with S_DNGD = 1.37–2.38; the CNGD and FNGD are markedly lower, with S_CNGD = 0.006–0.77 and S_FNGD = 0.004–0.88. On average, the DNGD sensitivity is about 3 times that of the CNGD and FNGD. Table 4 shows the density errors calculated in limestone with different densities and HI, indicating that all NGD algorithms can eliminate the influence of HI.

**Table 3.** Normalized relative sensitivity of three NGD algorithms.

| DNGD (g/cm$^3$) | S_DNGD | CNGD (g/cm$^3$) | S_CNGD | FNGD (g/cm$^3$) | S_FNGD |
|---|---|---|---|---|---|
| 2.6791 | 2.3800 | 2.6886 | 0.0060 | 2.7089 | 0.0040 |
| 2.6393 | 1.8200 | 2.6349 | 0.1790 | 2.6318 | 0.1400 |
| 2.5646 | 1.6300 | 2.5568 | 0.4730 | 2.5404 | 0.4470 |
| 2.4622 | 1.6960 | 2.4597 | 0.6510 | 2.4476 | 0.6560 |
| 2.3657 | 1.7290 | 2.3759 | 0.6870 | 2.3620 | 0.7310 |
| 2.2798 | 1.7950 | 2.2797 | 0.7410 | 2.2793 | 0.8400 |
| 2.1921 | 1.7780 | 2.1909 | 0.7680 | 2.1988 | 0.8540 |
| 2.1218 | 1.5630 | 2.1104 | 0.7350 | 2.1266 | 0.8440 |
| 2.0409 | 1.3660 | 2.0252 | 0.7460 | 2.0534 | 0.8810 |

**Table 4.** Density errors calculated in limestone with different densities and HI.

| Limestone with Different Densities and HI | | | | | | | |
|---|---|---|---|---|---|---|---|
| HI | Error (g/cm$^3$) | | | HI | Error (g/cm$^3$) | | |
| | DNGD | CNGD | FNGD | | DNGD | CNGD | FNGD |
| 0.01 | 0.0138 | 0.0043 | 0.0160 | 0.01 | 0.0319 | 0.0045 | 0.0438 |
| 0.05 | 0.0148 | 0.0104 | 0.0073 | | 0.0323 | 0.0180 | 0.0314 |
| 0.10 | 0.0256 | 0.0178 | 0.0014 | 0.10 | 0.0244 | 0.0141 | 0.0200 |
| 0.15 | 0.0087 | 0.0062 | 0.0059 | | 0.0228 | 0.0047 | 0.0403 |
| 0.20 | 0.0023 | 0.0079 | 0.0060 | 0.20 | 0.0026 | 0.0106 | 0.0003 |
| 0.25 | 0.0027 | 0.0028 | 0.0032 | | 0.0180 | 0.0063 | 0.0338 |
| 0.30 | 0.0049 | 0.0061 | 0.0018 | 0.30 | 0.0100 | 0.0070 | 0.0093 |
| 0.35 | 0.0103 | 0.0011 | 0.0151 | | 0.0029 | 0.0040 | 0.0112 |
| 0.40 | 0.0149 | 0.0009 | 0.0274 | 0.40 | 0.0062 | 0.0032 | 0.0239 |
| | | | | | 0.0054 | 0.0090 | 0.0113 |

### *3.4. Gas-Bearing Formations*

The formation of the model is changed to limestone with porosities of 1% to 40%. The pore fluid is a mixture of $CH_4$ and freshwater, and the $CH_4$ saturation is set at 60%, 80%, and 100%. Figure 7 shows the application results of the NGD algorithms in gas-bearing formations.

As shown in Table 5, the DNGD and FNGD can accurately calculate density in gas-bearing formations, while the CNGD has large density errors. Taking 40% limestone with a gas saturation of 100% as an example, the density errors of the CNGD, DNGD, and FNGD are 0.1123 g/cm$^3$, 0.0345 g/cm$^3$, and 0.0307 g/cm$^3$. The reason for the density errors in the CNGD is that fast neutrons and thermal neutrons have different response laws in gas-bearing formations. Thermal neutrons have an excavation effect in gas-bearing formations, while high-energy fast neutrons do not [36]. The production of capture gamma rays is closely related to thermal neutrons. As a result, the NGD algorithms using the

capture gamma or thermal neutron information are all affected by the excavation effect in gas-bearing formations.

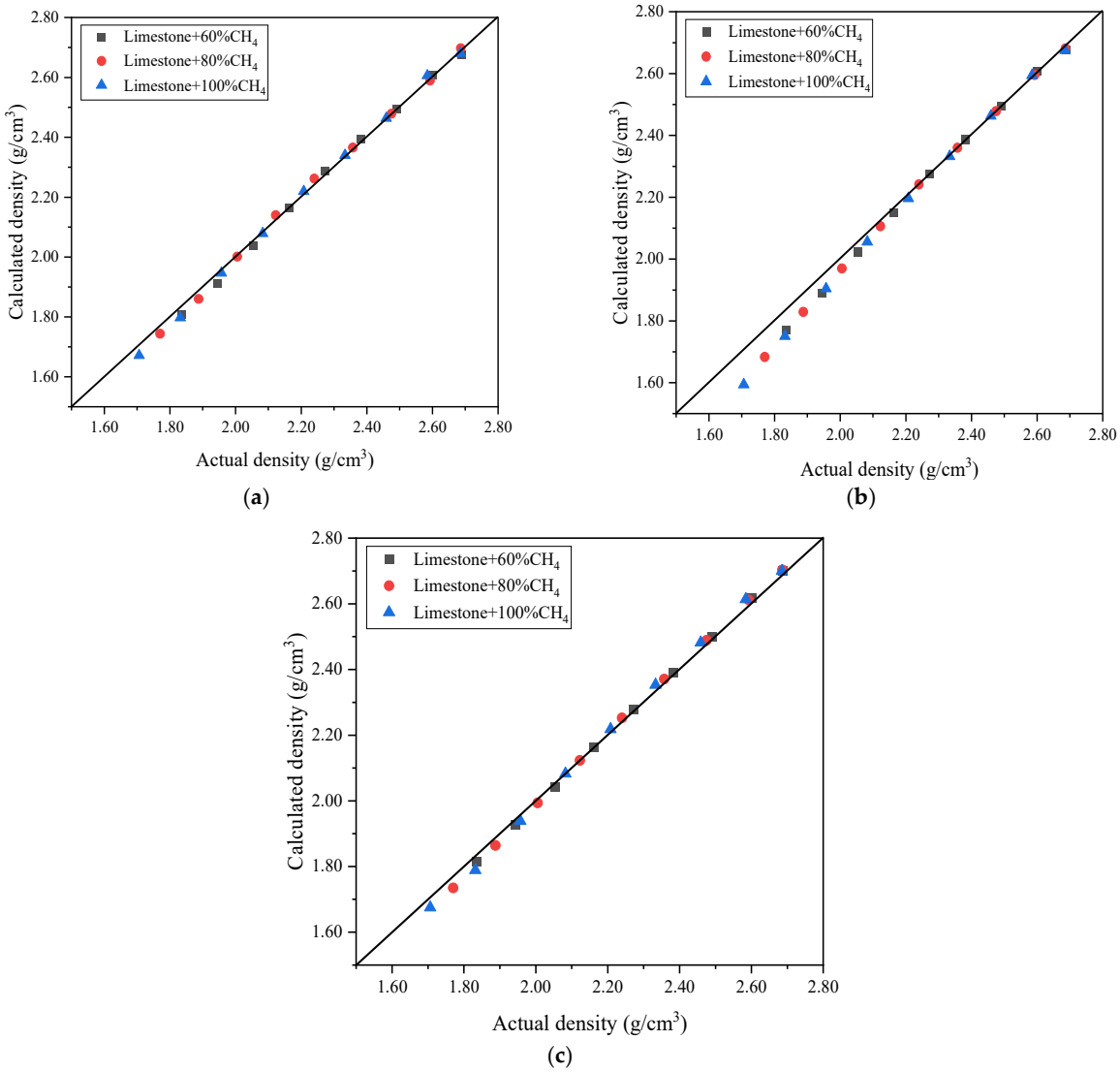



**Figure 7.** Calculated density results for gas-bearing formations. (**a**) Results of the DNGD in gas-bearing formations. (**b**) Results of the CNGD in gas-bearing formations. (**c**) Results of the FNGD in gas-bearing formations.

**Table 5.** Density errors calculated in gas-bearing formations.

| Porosity (%) | Limestone + 60%$CH_4$ | | | Limestone + 80%$CH_4$ | | | Limestone + 100%$CH_4$ | | |
|---|---|---|---|---|---|---|---|---|---|
| | Error (g/cm$^3$) | | | Error (g/cm$^3$) | | | Error (g/cm$^3$) | | |
| | DNGD | CNGD | FNGD | DNGD | CNGD | FNGD | DNGD | CNGD | FNGD |
| 1 | 0.0108 | 0.0094 | 0.0137 | 0.0107 | 0.0055 | 0.0171 | 0.0045 | 0.0098 | 0.0149 |
| 5 | 0.0059 | 0.0090 | 0.0189 | 0.0028 | 0.0029 | 0.0190 | 0.0216 | 0.0097 | 0.0298 |
| 10 | 0.0046 | 0.0042 | 0.0102 | 0.0037 | 0.0034 | 0.0136 | 0.0046 | 0.0040 | 0.0229 |
| 15 | 0.0122 | 0.0053 | 0.0087 | 0.0083 | 0.0026 | 0.0136 | 0.0065 | 0.0012 | 0.0197 |
| 20 | 0.0149 | 0.0042 | 0.0066 | 0.0220 | 0.0014 | 0.0126 | 0.0113 | 0.0119 | 0.0103 |
| 25 | 0.0010 | 0.0134 | 0.0016 | 0.0174 | 0.0160 | 0.0008 | 0.0037 | 0.0270 | 0.0005 |
| 30 | 0.0139 | 0.0292 | 0.0105 | 0.0035 | 0.0353 | 0.0111 | 0.0104 | 0.0524 | 0.0184 |
| 35 | 0.0305 | 0.0534 | 0.0166 | 0.0272 | 0.0587 | 0.0234 | 0.0340 | 0.0811 | 0.0425 |
| 40 | 0.0272 | 0.0629 | 0.0203 | 0.0261 | 0.0869 | 0.0351 | 0.0345 | 0.1123 | 0.0307 |

### *3.5. High-Salinity Formations*

The formation of the model is changed to water-saturated limestone with porosities of 1% to 40%. And the water salinity is set to 100 kppm, 150 kppm, and 200 kppm. Figure 8 shows the results of applying NGD algorithms in high-salinity formations.

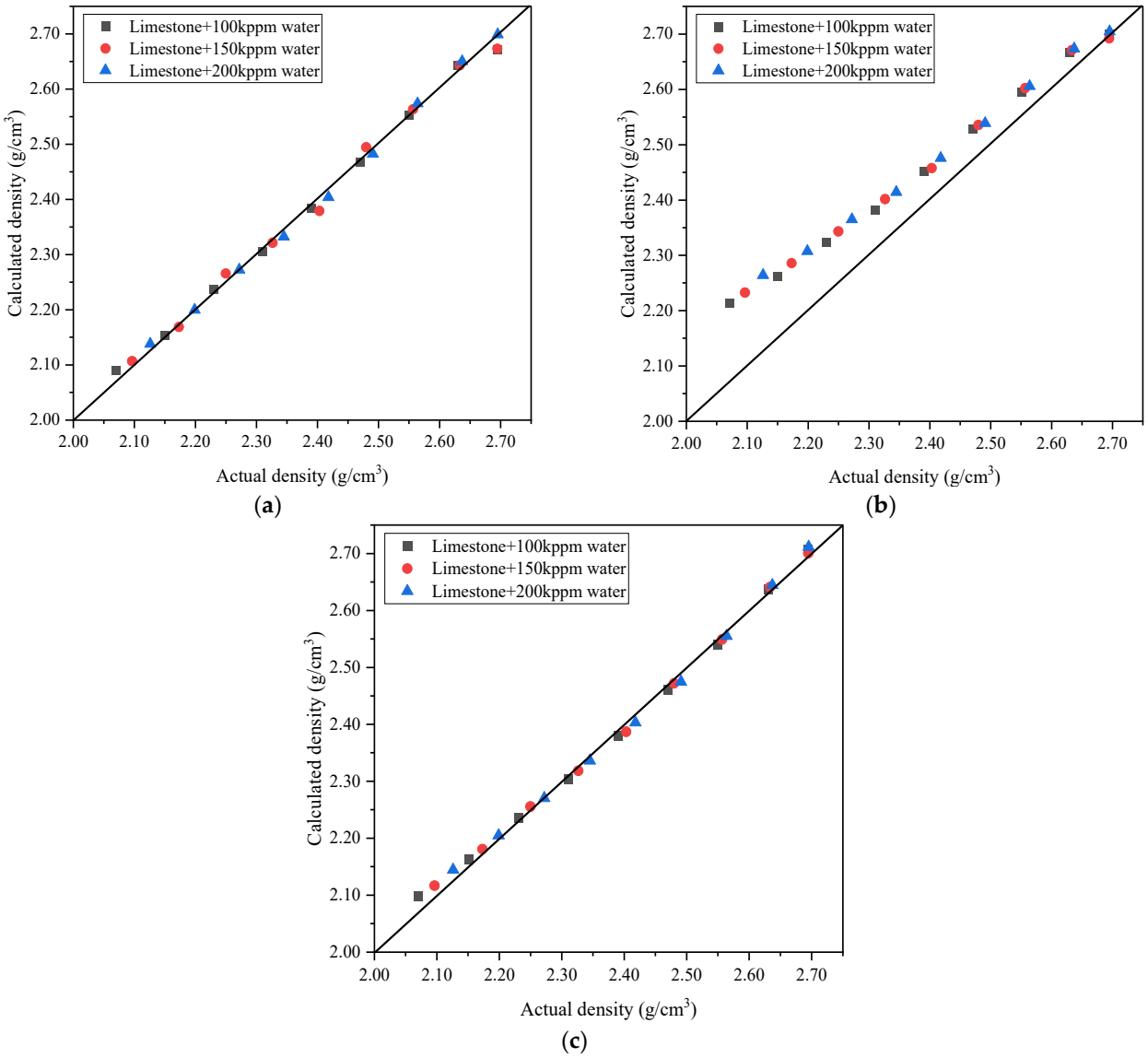



**Figure 8.** Calculated density results for high-salinity formations. (**a**) Results of the DNGD in high-salinity formations. (**b**) Results of the CNGD in high-salinity formations. (**c**) Results of the FNGD in high-salinity formations.

As shown in Table 6, the DNGD and FNGD can accurately calculate density in high-salinity formations. However, the density error of the CNGD increases with increasing porosity. Taking 40% limestone with a salinity of 200 kppm as an example, the density errors of the CNGD, DNGD, and FNGD are 0.1381 g/cm$^3$, 0.0119 g/cm$^3$, and 0.0185 g/cm$^3$. The generation and distribution of captured gamma rays are significantly influenced by salinity. The impact of salinity is introduced into the density error when the CNGD uses capture gamma.

**Table 6.** Density errors calculated in high-salinity formations.

| Porosity (%) | Salinity: 100 kppm | | | Salinity: 150 kppm | | | Salinity: 200 kppm | | |
|---|---|---|---|---|---|---|---|---|---|
| | Error (g/cm$^3$) | | | Error (g/cm$^3$) | | | Error (g/cm$^3$) | | |
| | DNGD | CNGD | FNGD | DNGD | CNGD | FNGD | DNGD | CNGD | FNGD |
| 1 | 0.0222 | 0.0056 | 0.0122 | 0.0216 | 0.0024 | 0.0058 | 0.0035 | 0.0092 | 0.0162 |
| 5 | 0.0124 | 0.0372 | 0.0070 | 0.0100 | 0.0378 | 0.0075 | 0.0132 | 0.0365 | 0.0075 |
| 10 | 0.0026 | 0.0450 | 0.0095 | 0.0068 | 0.0457 | 0.0075 | 0.0099 | 0.0417 | 0.0090 |
| 15 | 0.0020 | 0.0583 | 0.0084 | 0.0146 | 0.0558 | 0.0078 | 0.0088 | 0.0479 | 0.0164 |
| 20 | 0.0055 | 0.0614 | 0.0096 | 0.0240 | 0.0544 | 0.0161 | 0.0141 | 0.0578 | 0.0149 |
| 25 | 0.0053 | 0.0710 | 0.0063 | 0.0052 | 0.0751 | 0.0080 | 0.0126 | 0.0693 | 0.0088 |
| 30 | 0.0077 | 0.0932 | 0.0056 | 0.0160 | 0.0936 | 0.0058 | 0.0004 | 0.0930 | 0.0015 |
| 35 | 0.0033 | 0.1110 | 0.0128 | 0.0043 | 0.1129 | 0.0078 | 0.0008 | 0.1087 | 0.0059 |
| 40 | 0.0196 | 0.1428 | 0.0278 | 0.0105 | 0.1364 | 0.0203 | 0.0119 | 0.1381 | 0.0185 |

## 4. Application Analysis

This study employs the Monte Carlo method to study the influence of environmental factors such as the borehole, lithology, and shale on the DNGD.

### *4.1. Borehole Environment Effects*

The influence of the borehole environment on the DNGD is studied by varying the borehole size and the density of the mud. The borehole is filled with mud. The borehole size is set to 20 cm and 30 cm, with mud densities set at 1.00 g/cm$^3$, 1.30 g/cm$^3$, and 1.60 g/cm$^3$.

The influence of the borehole environment on the DNGD is shown in Figure 9. The NGD instrument measures the average density of the borehole and the surrounding formation. When the borehole size is 20 cm, the proportion of borehole fluid is small, resulting in a smaller impact of the borehole fluid on density calculations. However, when the borehole size increases to 30 cm, the proportion of borehole fluid within the entire detection range of the tool increases, and the influence of mud density on the density results becomes apparent. Therefore, when studying the influence of the borehole environment on the DNGD, both borehole size and mud density need to be considered.

$$\Delta\rho_{\mathrm{mud,bore}} = -0.0122(D_{\mathrm{bore}} - 20) + 0.0564(\rho_{\mathrm{mud}} - 1.0) + 0.0102(D_{\mathrm{bore}} - 20)(\rho_{\mathrm{mud}} - 1.0) \quad (15)$$

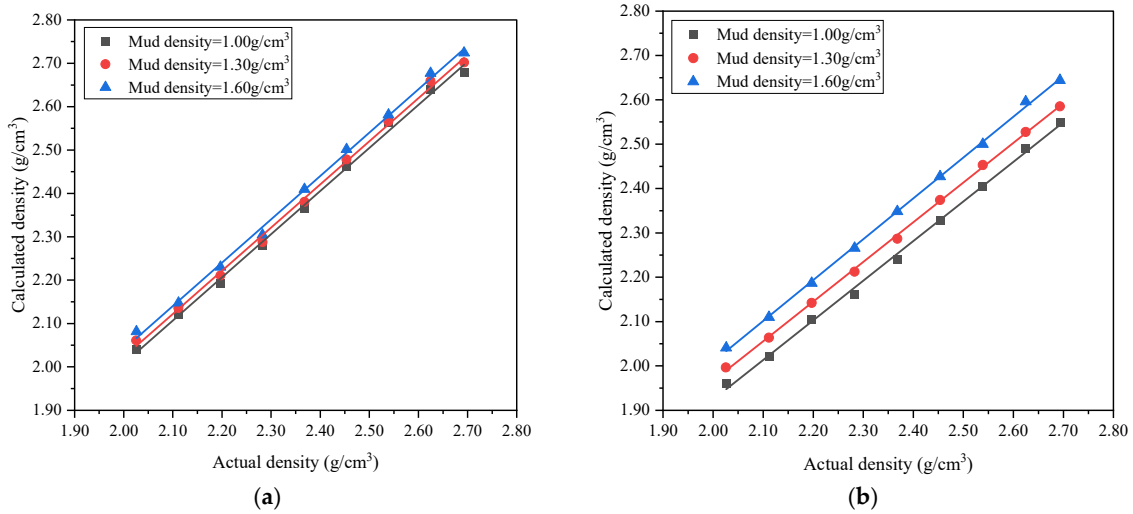



**Figure 9.** The effect of borehole environment on DNGD. (**a**) Borehole size is 20 cm. (**b**) Borehole size is 30 cm.

In Equation (15), $\Delta\rho_{mud,bore}$ is the correction amount for the borehole environment, $\rho_{mud}$ is the mud density, and $D_{bore}$ is the borehole size. The DNGD algorithm is calibrated using a borehole size of 20 cm and a mud density of 1.00 g/cm$^3$ as the standard. When calibrating the borehole environment, both the borehole size and mud density need to be considered. Therefore, a borehole environment calibration formula is formed by establishing a relationship between density error and borehole size and mud density. This formula can be used to correct both the borehole size and mud density.

### *4.2. Lithology Effects*

The formation of the model is changed to a freshwater-saturated limestone with porosities of 1% to 40%, a freshwater-saturated sandstone with porosities of 1% to 40%, and a freshwater-saturated dolomite with porosities of 1% to 40%. The formation density is calculated using the DNGD and the results are shown in Figure 10.

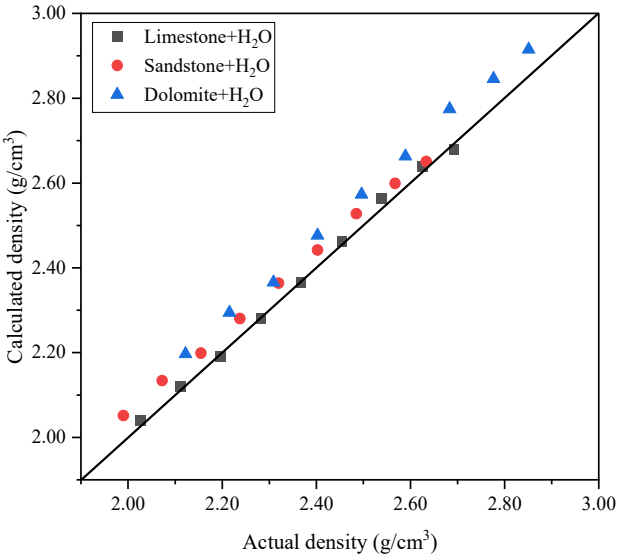



**Figure 10.** The effect of different lithologies on DNGD.

The DNGD is affected by lithologies. The reason for the error is that different elements produce different inelastic gamma rays. While the inelastic gamma rays produced by the drill collar can correct for the fast neutron distribution, the drill-collar inelastic gamma cannot compensate for density errors caused by differences in elements.

$$\Delta\rho_{\text{lith}} = \begin{cases} 0 \text{ (limestone)} \\ 0.043 \text{(sandstone)} \\ 0.073 \text{ (dolomite)} \end{cases} \quad (16)$$

In Equation (16), $\Delta\rho_{lith}$ is the correction amount for lithology. The DNGD algorithm uses limestone as the baseline scale, and changes in lithology will cause deviations in the calculated density. Therefore, limestone does not require correction, sandstone is approximately +0.043 g/cm$^3$, and dolomite is approximately +0.073 g/cm$^3$.

### *4.3. Shale Effects*

The formation of the model is changed to a freshwater-saturated limestone with porosities of 1% to 40%. The shale was set to kaolinite, with shale content set to 0%, 20%, and 40%. The formation density is calculated using the DNGD and the results are shown in Figure 11.

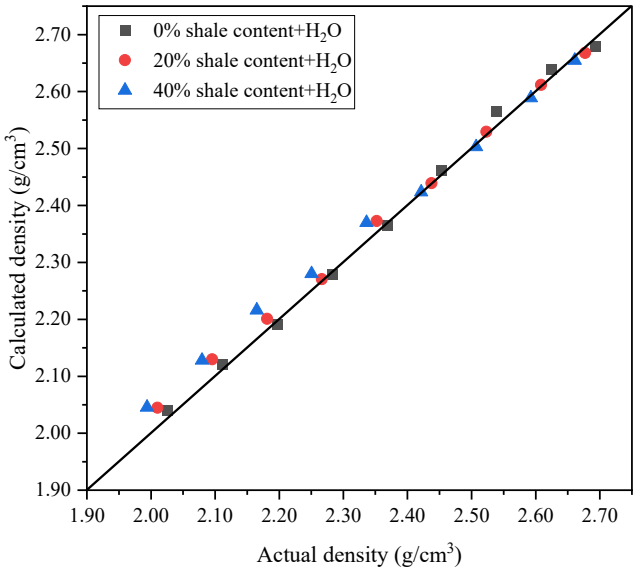



**Figure 11.** The effect of shale on DNGD.

The DNGD is affected by the presence of shale. Similar to lithology, shale contains elements such as aluminum and sodium, leading to significant differences in inelastic gamma responses between shale and limestone. Therefore, using the DNGD in the presence of shale may lead to errors in density measurements.

$$\Delta\rho_{\text{shale}} = -0.038 \cdot V_{\text{sh}} \tag{17}$$

In Equation (17), $\Delta\rho_{shale}$ is the correction amount for shale, and $V_{sh}$ is the shale content. By establishing the relationship between shale content and density error, a shale correction formula was obtained. This formula can be used to correct the influence of shale on the DNGD algorithm.

### *4.4. Tool Eccentricity Effect*

The formation of the model is changed to a freshwater-saturated limestone with porosities of 1% to 40%. Tool eccentricity is set to 0.5 cm, 0.0 cm, and −0.5 cm. The formation density is calculated using the DNGD and the results are shown in Figure 12.

Since the density algorithm uses an eccentricity scale of e = 0.5 cm, the detector is closest to the formation at this point, and the mud layer is thinnest in the middle, so the calibrated density equals the actual density of the formation. As the tool moves towards the center of the wellbore, the mud layer between the detector and the formation thickens; the mud is much lighter than the formation and attenuates the non-elastic gamma of the drill collar, weakening the detector signal. The calibration formula interprets this as a lower density.

$$\Delta\rho_{\text{ecc}} = 0.0058 \cdot (5 - |e|) \tag{18}$$

In Equation (18), $\Delta\rho_{ecc}$ is the correction amount for tool eccentricity, and $e$ is the tool eccentricity. The DNGD algorithm is calibrated at e = 0.5 cm. By establishing the relationship between tool eccentricity and density error, a tool eccentricity density correction formula is derived. This formula can be used to correct the influence of eccentricity on the DNGD algorithm.

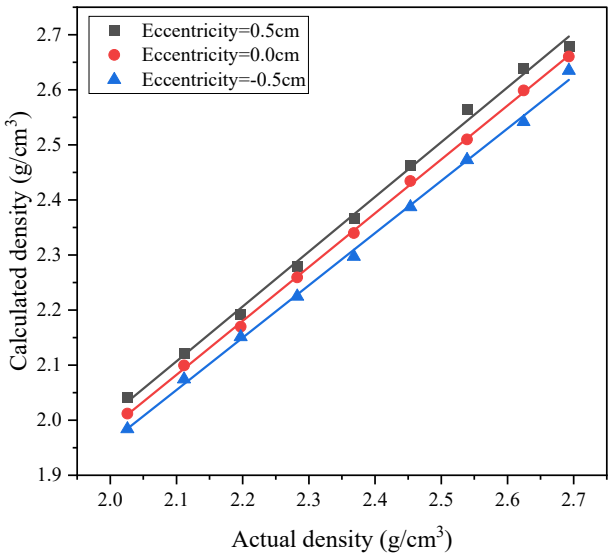



**Figure 12.** The effect of tool eccentricity on DNGD.

### *4.5. Drill-Collar Diameter Effect*

The formation of the model is changed to a freshwater-saturated limestone with porosities of 1% to 40%. The diameters of the drill collars were set to 19.0 cm, 20.0 cm, and 21.0 cm. The formation density is calculated using the DNGD and the results are shown in Figure 13.

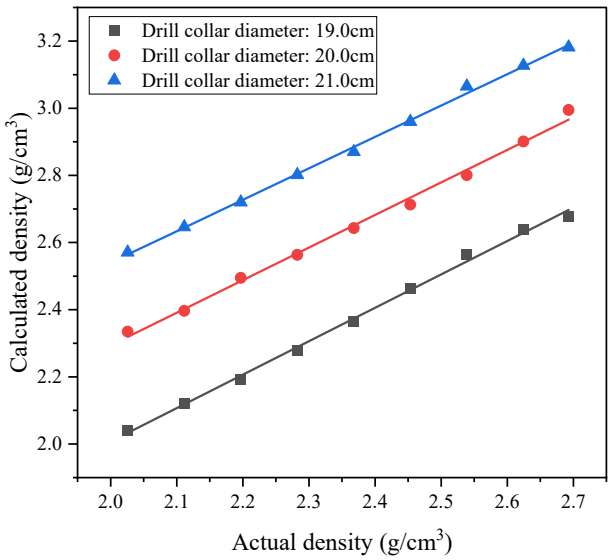



**Figure 13.** The effect of drill-collar diameter on DNGD.

When the drill-collar diameter increases, the calculated density increases. This is because the DNGD method calculates the average density. Since the drill collar is by far the densest component, its increased weighting raises the effective average density sensed by the detector. The calibration formula is calibrated with a fixed drill-collar diameter, making the DNGD response sensitive to the drill-collar diameter.

$$\Delta\rho_{\text{coll}} = 0.260 \cdot (D - 19) \tag{19}$$

In Equation (19), $\Delta\rho_{coll}$ is the correction amount for drill-collar diameter and $D$ is the drill-collar diameter. The DNGD algorithm is calibrated at D = 19.0 cm. By establishing the relationship between drill-collar diameter and density error, a drill-collar diameter

density correction formula is derived. This formula can be used to correct the influence of drill-collar diameter on the DNGD algorithm.

## 5. Discussion

*Advantages and Disadvantages*

As mentioned above, through the effective utilization of drill-collar inelastic gamma information, the new algorithm considerably improves the density sensitivity and accuracy of the NGD logging. Once the new algorithm is adopted, the NGD logging no longer requires extra corrections in saline and gas reservoirs, which is disruptive for the development of the entire NGD logging technology.

Of course, this new algorithm also has its own limitations. It depends on the accuracy of the drill-collar inelastic gamma information. Consequently, the new algorithm imposes higher requirements on both energy-spectrum quality and energy-spectrum analysis techniques. Currently, except for Schlumberger's NGD tool, which can provide high-quality energy-spectrum information [7], most NGD tools do not integrate elemental function. This limits the application of this new algorithm.

In recent years, integrating multiple logging functions has become a trend in the development of logging tools. In the future, when most NGD tools integrate elemental function, this new algorithm will play a more significant role in the NGD data processing.

## 6. Conclusions

To overcome the limitations of existing NGD algorithms, this study introduces the drill-collar inelastic gamma information into the NGD logging. Using the Monte Carlo simulation, the NGD logging responses were simulated, and the drill-collar inelastic gamma information was extracted by the spectral analysis techniques. The influence of drill-collar inelastic gamma information on NGD logging was studied, and the relationship between the drill-collar gamma information and high-energy fast neutrons was analyzed. Finally, a new NGD algorithm utilizing the drill-collar inelastic gamma information was established. The results are given as follows:

(1) The proportion of drill-collar inelastic gamma can exceed 50%, which is a significant factor leading to reduced density sensitivity.

(2) The drill-collar inelastic gamma can be obtained through spectral analysis techniques. By subtracting the influence of the drill-collar inelastic gamma, the density sensitivity of the new algorithm is significantly improved compared to the FNGD and CNGD.

(3) The drill-collar inelastic gamma shows a clear linear relationship with high-energy fast neutrons. The drill-collar inelastic gamma inherits the advantages of fast neutrons, and the detection efficiency of the drill-collar inelastic gamma is high. The new algorithm performs well compared to the CNGD in gas-bearing formations and high-salinity formations.

(4) The density results calculated by the new NGD algorithm are affected by the borehole environment, lithology, and shale.

(5) The new algorithm requires only two gamma detectors to achieve density measurement, requires no modifications to existing instruments, and can be used simultaneously with other NGD algorithms.

**Author Contributions:** Conceptualization, T.X. and Q.Z.; Methodology, T.X. and Q.Z.; Software, T.X., Q.Z., C.Y., G.L. and H.L.; Validation, T.X., Q.Z. and Y.H.; Formal analysis, Q.Z. and G.L.; Investigation, Q.Z.; Resources, Q.Z. and C.Y.; Data curation, T.X., C.Y., G.L., H.L. and Yin Huang; Writing – original draft, T.X.; Writing—review & editing, T.X. All authors have read and agreed to the published version of the manuscript.

**Funding:** This research was supported by the National Oil & Gas Major Project (2025ZD1401106).

**Institutional Review Board Statement:** Not applicable.

**Informed Consent Statement:** Not applicable.

**Data Availability Statement:** The original contributions presented in this study are included in the article. Further inquiries can be directed to the corresponding author.

**Conflicts of Interest:** Author Chao Yuan was employed by the PetroChina Oil, Gas & New Energies Company. The remaining authors declare that the research was conducted in the absence of any commercial or financial relationships that could be construed as a potential conflict.

## Abbreviations

The following abbreviations are used in this manuscript:

| | |
|---|---|
| NGD | Neutron–gamma density |
| LWD | Logging while drilling |
| D-T | Deuterium–tritium |
| FNGD | NGD algorithm based on fast neutron information |
| CNGD | NGD algorithm based on capture gamma information |
| ENGD | NGD algorithm based on epithermal neutron information |
| TNGD | NGD algorithm based on thermal neutron information |
| DNGD | NGD algorithm based on drill-collar inelastic gamma information |
| HI | Hydrogen index |
| MC | Monte Carlo |
| $LaBr_3$ | Lanthanum bromide |
| Nird | Near-detector drill-collar inelastic gamma count |
| $\Sigma s$ | Macroscopic scattering cross-section |
| S | Normalized relative sensitivity |

## References

1. Aitken, J.D.; Adolph, R.; Evans, M.; Wijeyesekera, N.; McGowan, R.; Mackay, D. Radiation sources in drilling tools: Comprehensive risk analysis in the design, development and operation of LWD tools. In Proceedings of the SPE International Conference on Health, Safety and Environment in Oil and Gas Exploration and Production, Kuala Lumpur, Malaysia, 20–22 March 2002.
2. Badruzzaman, A.; Badruzzaman, T.; Zalan, T.A.; Mai, K. Multi-sensor through-casing density and saturation measurement concepts with a pulsed neutron source: A modeling assessment. In Proceedings of the SPE International Petroleum Conference in Mexico, Puebla, Mexico, 7–9 November 2004.
3. Badruzzaman, A.; Barnes, S.; Bair, F.; Grice, K. Radioactive sources in petroleum industry: Applications, concerns and alternatives. In Proceedings of the Asia Pacific Health, Safety, Security and Environment Conference, Jakarta, Indonesia, 4–6 August 2009.
4. Rafizade, A.; Hosseini, S.A. A novel framework for neutron-gamma density logging: Semi-empirical modeling, directional neutron sources, and experimental benchmarking. *Sci. Rep.* **2025**, *15*, 19895. [CrossRef] [PubMed]
5. Dong, D.; Wu, W.S.; Yue, W.Z.; Ge, Y.; Xiong, S.; Zhao, W.; Wang, R. Improving the pulsed neutron-gamma density method with machine learning regression algorithms. *J. Pet. Sci. Eng.* **2022**, *218*, 110962. [CrossRef]
6. Zhang, Q.; Ge, Y.; Li, Y.L. Source-less density measurement using an adaptive neutron-induced gamma correction method. *Nucl. Sci. Tech.* **2023**, *34*, 125. [CrossRef]
7. Mauborgne, M.-L.; Rodriguez, R.; Allioli, F.; Sergeyeva, V.; Haranger, F.; Pallain, A.; Babaghayou, I.; Tanguy, E.; Jain, V.; Agarwal, V.; et al. Enhancing accuracy and range of sourceless density. *Petrophysics* **2024**, *65*, 929–943. [CrossRef]
8. Yu, H.W.; Wang, Z.; Zhang, Q.W.; Xue, Z.B.; Shang, X.S.; Yuan, W.; Li, S.D.; Wang, C. Data-processing methods for D–T source neutron-gamma density logging while drilling. *Nucl. Sci. Tech.* **2025**, *36*, 93. [CrossRef]
9. Wilson, R.D. Bulk density logging with high-energy gammas produced by fast neutron reactions with formation oxygen atoms. In Proceedings of the IEEE Nuclear Science Symposium and Medical Imaging Conference Record, San Francisco, CA, USA, 21–28 October 1995.
10. Archer, M.P.; Odom, R.C.; Wilson, R.D.; Bailey, S.M. Pulsed neutron density measurements: Modeling the depth of investigation and cased-hole borehole uncertainties. In Proceedings of the SPWLA 40th Annual Logging Symposium, Oslo, Norway, 30 May–3 June 1999.

11. Odom, R.C.; Wilson, R.D.; Ladtkow, R.K. Log examples with a prototype three-detector pulsed-neutron system for measurement of cased-hole neutron and density porosities. In Proceedings of the SPE Rocky Mountain Petroleum Technology Conference, Keystone, PA, USA, 21–23 May 2001.
12. Reichel, N.; Evans, M.; Allioli, F.; Mauborgne, M.-L.; Nicoletti, L.; Haranger, F.; Laporte, N.; Stoller, C.; Cretoiu, V.; El Hehiawy, E.; et al. Neutron-gamma density (NGD): Principles, field test results and log quality control of a radioisotope-free bulk density measurement. In Proceedings of the SPWLA 53rd Annual Logging Symposium, Cartagena, Colombia, 16–20 June 2012.
13. Allioli, F.; Cretoiu, V.; Mauborgne, M.-L.; Evans, M.; Griffiths, R.; Haranger, F.; Stoller, C.; Murray, D.; Reichel, N. Formation density from a cloud, while drilling. *Oilfield Rev.* **2013**, *25*, 4–15.
14. Chen, J.Y.; Zhang, Q. Neutron-gamma density measurement method using the mass attenuation coefficient function. *Nucl. Sci. Tech.* **2026**, *37*, 9.
15. Wang, H.; Yue, A.Z.; Zhang, X.L.; Tang, J.; He, X.; Luo, X.; Han, B. Bulk density response and experimental study of pulsed neutron-gamma density logging. *Front. Earth Sci.* **2022**, *10*, 803775. [CrossRef]
16. Al-Mudhaf, M.; Al-Fayez, F.; Alasaker, H.; Al-Saeedi, A.M.; Al-Samhan, S.; Saleem, A.; Azmi, S.M.; Aldhafeeri, O.F.; Ali Haji, D.; Dasgupta, S.; et al. Sourceless logging while drilling platform enables reservoir evaluation in complex and high-risk drilling environment: A case study from Abdali and Ahmadi Field, Kuwait. In Proceedings of the ADIPEC, Abu Dhabi, United Arab Emirates, 3–6 November 2025.
17. Luycx, M.; Torres-Verdín, C. Resolution and accuracy of neutron-gamma density measurements compared to conventional gamma-gamma density measurements. In Proceedings of the SPE Annual Technical Conference and Exhibition, San Antonio, TX, USA, 9–11 October 2017.
18. Luycx, M.; Torres-Verdín, C. Physics, applications, and limitations of borehole neutron-gamma density measurements. *Geophysics* **2019**, *84*, D39–D56. [CrossRef]
19. Zhang, Q.Y. Research on Pulsed Neutron Dual-Spectrum Density Logging Method Based on D-T Neutron Source. Master's Thesis, China University of Petroleum (East China), Qingdao, China, 2019.
20. Zhang, L.; Yu, H.W.; Li, Y.; Jia, W.B.; Han, X.; Geng, X.S. Improved formation density measurement using controllable D-D neutron source and its lithological correction for porosity prediction. *Nucl. Sci. Tech.* **2022**, *33*, 3. [CrossRef]
21. Jacobson, L.; Durbin, D.; Reed, S. An improved formation density measurement using PNC tools. In Proceedings of the SPE Annual Technical Conference and Exhibition, Houston, TX, USA, 26–29 September 2004.
22. Quirein, J.; Smith, H.; Chen, D.; Perkins, T.; Reed, S. Formation density prediction using pulsed neutron capture tools. In Proceedings of the SPWLA 46th Annual Logging Symposium, New Orleans, LA, USA, 26–29 June 2005.
23. Mirto, E.; Weller, G.; el-Halawani, T.; Grau, J.; Berheide, M.; Allioli, F.; Evans, M.; Berto, R.; Borghi, M.; Firinu, M.; et al. New developments in sourceless logging-while-drilling formation evaluation: A case study from Southern Italy. In Proceedings of the SPE Europec/EAGE Annual Conference and Exhibition, Vienna, Austria, 12–15 June 2006.
24. Yu, H.W.; Sun, J.M.; Wang, J.X.; Gardner, R. Accuracy and borehole influences in pulsed neutron gamma density logging while drilling. *Appl. Radiat. Isot.* **2011**, *69*, 1313–1317. [CrossRef] [PubMed]
25. Evans, M.; Allioli, F.; Cretoiu, V.; Haranger, F.; Laporte, N.; Mauborgne, M.-L.; Nicoletti, L.; Reichel, N.; Stoller, C.; Tarrius, M.; et al. Sourceless neutron-gamma density (SNGD): A radioisotope-free bulk density measurement: Physics principles, environmental effects, and applications. In Proceedings of the SPE Annual Technical Conference and Exhibition, San Antonio, TX, USA, 8–10 October 2012.
26. Al-Rubaiyea, J.; Al-Bader, A.; Al-Houli, M.; Al-Najim, A.; Al-Duwaish, M.; Elsherif, A. An innovative approach to formation evaluation with a sourceless LWD technology: A case study from partitioned zone between Kuwait and Saudi Arabia. In Proceedings of the SPE Middle East Intelligent Oil and Gas Conference and Exhibition, Abu Dhabi, United Arab Emirates, 15–16 September 2015.
27. Wang, H.; Wu, W.S.; Tang, T.Z.; Wang, R.; Yue, A.; Wang, S.; Yang, C.; Fu, X. A new method for calculating bulk density in pulsed neutron-gamma density logging. *Geophysics* **2020**, *85*, D219–D232. [CrossRef]
28. Rafizade, A.; Hosseini, S.A. Modeling and simulation of neutron-gamma density logging: Impact of mudcake thickness and barite content on measurement accuracy. *Nucl. Eng. Technol.* **2026**, *58*, 103883. [CrossRef]
29. Xing, G.J.; Zhang, Q.Y.; Li, N.C.; Zhang, F.; Liu, G.B. A LWD gas-reservoir recognition method based on the inelastic gamma information of the drill collar. *Geoenergy Sci. Eng.* **2023**, *225*, 211684. [CrossRef]
30. Zhang, Q.Y.; Zhang, F.; Liu, J.T.; Wang, X.; Wu, H.; Jia, W.; Ti, Y.; Qiu, F.; Zhang, X. A method to describe inelastic gamma field distribution in neutron gamma density logging. *Appl. Radiat. Isot.* **2017**, *129*, 189–195. [CrossRef] [PubMed]
31. Zhang, F.; Zhang, Q.Y.; Liu, J.T.; Wu, H.; Wu, G.; Jia, W.; Ti, Y.; Li, J. A method of determining formation density based on fast-neutron gamma coupled field theory. *Petrophysics* **2017**, *58*, 411–425.
32. Zhang, Q.Y.; Zhang, F.; Yuan, C.; Deng, R.; Liu, G. Application analysis on the different neutron gamma density (NGD) logging methods. *Appl. Radiat. Isot.* **2021**, *172*, 109672. [CrossRef] [PubMed]

33. Galford, J.; Truax, J.; Hrametz, A.; Haramboure, C. A new neutron-induced gamma-ray spectroscopy tool for geochemical logging. In Proceedings of the SPWLA 50th Annual Logging Symposium, The Woodlands, TX, USA, 21–24 June 2009.
34. Herron, S.; Herron, M.; Pirie, I.; Saldungaray, P.; Craddock, P.; Charsky, A.; Polyakov, M.; Shray, F.; Li, T. Application and quality control of core data for the development and validation of elemental spectroscopy log interpretation. *Petrophysics* **2014**, *55*, 392–414.
35. Haranger, F.; Allioli, F.; Berheide, M.; Craddock, P.; Øpsen, D.F.; Grau, J.; Horstmann, M.; Maggs, D.; Mauborgne, M.-L.; Pallain, A.; et al. A step change in neutron-induced gamma ray spectroscopy: Using a high-resolution LABR3:Ce detector in an integrated LWD tool. In Proceedings of the SPWLA 64th Annual Logging Symposium, Lake Conroe, TX, USA, 10–14 June 2023.
36. Segesman, F.; Liu, O. The Excavation Effect. In *Transactions of the SPWLA 12th Annual Logging Symposium*; SPWLA: Dallas, TX, USA, 1971.

**Disclaimer/Publisher's Note:** The statements, opinions and data contained in all publications are solely those of the individual author(s) and contributor(s) and not of MDPI and/or the editor(s). MDPI and/or the editor(s) disclaim responsibility for any injury to people or property resulting from any ideas, methods, instructions or products referred to in the content.